NANO · MICRO small
www.small-journal.com

Heterocarbides Reinforced Electrochemical Energy Storage

Jing Cuan, Fan Zhang, Yang Zheng, Tengfei Zhou, Gemeng Liang, Zaiping Guo, Wei Kong Pang, and Xuebin Yu**

The feasibility of transition metal carbides (TMCs) as promising high-rate electrodes is still hindered by low specific capacity and sluggish charge transfer kinetics. Improving charge transport kinetics motivates research toward directions that would rely on heterostructures. In particular, heterocomposing with carbon-rich TMCs is highly promising for enhancing Li storage. However, due to limited synthesis methods to prepare carbon-rich TMCs, understanding the interfacial interaction effect on the high-rate performance of TMCs is often neglected. In this work, a novel strategy is proposed to construct a binary carbide heteroelectrode, i.e. incorporating the carbon-rich TMC (M=Mo) with its metal-rich TMC nanowires (nws) via an ingenious in situ disproportionation reaction. Results show that the as-prepared MoC-Mo_2C-heteronanowires (hnws) electrode could fully recover its capacity after high-rates testing, and also possesses better lithium accommodation performance. Kinetic analysis verified that both electron and ion transfer in MoC-Mo_2C-hnws are superior to those of its singular counterparts. Such improvements suggest that by taking utilization of the interfacial component interactions of stoichiometry tunable heterocarbides, the electrochemical performance, especially high-rate capability of carbides, could be significantly enhanced.

The ever-growing global energy consumption, coupled with concerns on environmental pollution, are placing urgent demands on clean and renewable energy sources.[1–3] Rechargeable batteries are attractive energy storage technologies and offer great opportunities for sustainable energy storage applications in smart grids.[4,5] Of particular, lithium-ion batteries (LIBs) have been extensively developed and witnessed giant popularity in the markets of diverse portable electronics and electric vehicles/hybrid electric vehicles over the past several decades.[6–9] However, the expanded applications of LIBs for heavy vehicles or machines demand high power outputs, and are still impeded by the behindhand performances in deteriorating performances at high current density, low Li capacity, and nonideal battery duration, which are ultimately associated with challenges for fabricating high-rate electrodes.[10,11] Toward the ingenious design of high-rate electrodes, several basic requirements have been reported, by which the integrated multifunctions are anticipated to cover these shortages:[12,13] (1) in-built high conductive electronic pathways; (2) porous features to enhance the electrolyte infiltration and improve ionic diffusion; (3) selecting materials with excellent mechanical strength and good corrosion resistance to form robust skeletons, which could alleviate volume expansions and prevent detrimental etching of the by-products during cycling.

In this regard, transition metal carbides (TMCs) could be reckoned as a fascinating class of candidates, in consideration of their non-Faradaic and Faradaic charge-storage capability, high conductive compositions (carbon atoms distributed in host transition metal skeleton voids), and favorable attributes involving chemical/mechanical stability, and abundant catalytic sites.[14] Such merits of TMCs consequently contribute to

J. Cuan, F. Zhang, Prof. X. B. Yu
Department of Materials Science
Fudan University
Shanghai 200433, China
E-mail: yuxuebin@fudan.edu.cn

J. Cuan, Dr. Y. Zheng, Dr. T. Zhou, G. Liang, Prof. Z. P. Guo, Dr. W. K. Pang
Institute for Superconducting and Electronic Materials
School of Mechanical
Materials and Mechatronics Engineering
University of Wollongong
Wollongong 2511, NSW, Australia
E-mail: zguo@uow.edu.au

The ORCID identification number(s) for the author(s) of this article can be found under https://doi.org/10.1002/smll.201903652.

Dr. Y. Zheng
Institute for Advanced Materials and Nanotechnology
The State Key Laboratory of Refractories and Metallurgy
Wuhan University of Science and Technology
Wuhan 430081, P. R. China

Dr. T. Zhou
College of Chemistry and Materials Science
South-Central University for Nationalities
Wuhan 430074, China

Prof. Z. P. Guo
School of Mechanical
Materials and Mechatronics Engineering
University of Wollongong
Wollongong 2511, NSW, Australia

DOI: 10.1002/smll.201903652

fast rate response and support their feasibility as promising high-rate electrodes.[15,16] However, some TMCs, involving TiC, Fe_3C, V_2C, Nb_2C, etc., are often reported to accommodate Li^+ through intercalation pseudocapacitance or adsorption, resulting in low Li accommodation.[14] Following researches demonstrate that molybdenum carbide (Mo_2C), $Ni_3ZnC_{0.7}$, etc., could reversibly store Li^+ via two-phase conversion reactions (e.g., $Mo_2C + xLi^+ + xe^- \rightarrow 2Mo + Li_xC$), yielding higher Li theoretical capacity.[14] Of particular Mo_2C electrodes have favorable properties including high specific conductance (1.02×10^2 S cm^{-1}), suitable lithiation pathways, and similar d-band electronic density of states to Pt at the Fermi level, making the exploration of Mo_2C-based high-rate electrodes quite encouraging.[17,18] Moreover, extensive researches revealed that Mo_2C electrodes often exhibit ultrastable rate performances.[18–20] However, restricted by the metal-rich composition and poor Li solid-state diffusivity, Mo_2C electrodes often show undesirable Li storage capacity and sluggish charge transfer kinetics at high current density, which severely hinder their high-rate capability.[21] Notably, the impeded kinetic processes of electrodes, especially at fast lithiation/delithiation rates, in turn, threaten safety due to the generation of substantial heat.[22]

Diverse strategies have been attempted to improve the overall charge transport kinetics of Mo_2C, involving morphology control, creation of atomic defect sites, multiple-level structural engineering, interface integration, etc.[23–26] With respect to these strategies, forming composites allows an intriguing synergistic means to enhance ion transport among active phases,[27–29] as experimental and theoretical calculations have demonstrated that high-quality interfaces could induce effective charge redistribution,[30,31] leading to accelerated ionic/electronic diffusion kinetics.[32] For instances, Wang and co-workers verified the ultrafast charge transfer in MoS_2/WS_2 heterostructures using a photoluminescence mapping and femtosecond pump-probe spectroscopy.[33] The first-principle calculations conducted by Fan et al. illustrate that the heterostructured graphene/blue phosphorus has significantly enhanced Na absorption in comparison with its singular analogue.[34] This demonstrates that it is quite promising to regulate the charge transfer process by designing Mo_2C heterocomposite electrodes.

Moreover, improving the carbon chemical compositions in Mo_2C is anticipated to raise total Li storage capacity yet preserving the unique attributes of molybdenum carbide materials, since some recent pioneering work revealed that interactions between carbon and lithium contribute significantly to Li^+ accommodations of TMCs.[35] Whereas, due to limited synthesis method to prepare carbon-rich TMCs, understanding the interfacial interaction effect on the high-rate performance of TMCs is often neglected in previous research. Following these considerations, in this work, by incorporating high conductive carbon-rich MoC on Mo_2C nanowires, a binary carbide hetero-nanowire electrode has been prepared. As MoC keeps metallic and has higher theoretical capacity, its incorporation is anticipated to tailor the electrochemistry-related properties, of particular better capacity of Mo_2C at high rates.[36] The heteroelectrode was obtained using an in situ disproportionation strategy, which has several incomparable advantages in synthesis simplicity, relatively low prices, and convenience. Electrochemical investigations have demonstrated that the as-prepared MoC-Mo_2C-heteronanowires (MoC-Mo_2C-heterostructure nws (hnws)) have higher rate capacity and stability than single MoC-nanowires (nws) and Mo_2C-nws, and impressively, MoC-Mo_2C-hnws could resume its pristine capacity after rate testing. As verified by the electrochemical impedance spectroscopy and galvanostatic intermittent titration technique, the enhanced lithium storage performance and rate capability of MoC-Mo_2C-hnws should be attributed to the significantly improved charge transfer process within heterostructures, which is closely associated with synergistic coupling between MoC and Mo_2C in the interconnected architecture. The boosted Li-storage properties at high-rates demonstrate that the optimized strategy of structural engineering has good prospects to improve the power outputs of lithium-ion batteries.

MoC-Mo_2C-hnw composite was prepared via an in situ disproportionation reaction through calcining $Mo_3O_{10}(C_6H_8N)_2 \cdot 2H_2O$ precursor. Specifically, this process could be induced via a controlled carbothermal reaction described in **Figure 1**a. First, the good affinity between the ligands (organic units) and $Mo_7O_{24}^{6-}$ clusters (inorganic units) contributes to forming organic/inorganic hybrid building units, which subsequently replicate and organize themselves rapidly into long-range ordered $Mo_3O_{10}(C_6H_8N)_2 \cdot 2H_2O$ nanowires. The calcination of $Mo_3O_{10}(C_6H_8N)_2 \cdot 2H_2O$ gives rise to well-built heterogeneity between the in situ formed resultant products, MoC and Mo_2C phases. To conveniently compare the effects of the heterodesigned structure, both MoC-nws and Mo_2C-nws samples were fabricated. The detailed synthesis procedures have been provided in Method (Supporting Information). Examination using field-emission scanning electron microscopy (SEM) and transmission electron microscopy (TEM) demonstrated the well-aligned nanowire-type morphological features of $Mo_3O_{10}(C_6H_8N)_2 \cdot 2H_2O$ precursor and the as-prepared samples (Figure 1b,c,f,g,j,k and Figure S1, Supporting Information). As for MoC-Mo_2C-hnws (Figure 1b,c), the well-arranged side-by-side nanowires show smooth surfaces and average wire diameters of ≈110 nm, while the nanowires of Mo_2C-nws and MoC-nws have larger diameters and analogous appearance to those of MoC-Mo_2C-hnws (Figure 1f,g,j,k). The slight differences in sample morphologies may originate from divergent carbonization process of the identical nanowire precursor. In the high-resolution TEM image of MoC-Mo_2C-hnws, lattice fringe ≈0.212 nm (highlighted in white color) could be identified as the characteristic (2 0 0) plane of MoC phase, and the other set (highlighted in yellow color showing lattice fringe ≈0.236 nm) corresponds to the typical (2 0 0) planes of Mo_2C phase. As can be clearly observed (Figure 1 and Figure S1, Supporting Information), plenty of lattice interfaces exist in MoC-Mo_2C-hnws, for example, cross-linked $(200)_{Mo2C} \| (200)_{MoC}$ and adjacently arranged $(121)_{Mo2C} \| (200)_{MoC}$ interfaces, etc., manifesting a close contact between MoC and Mo_2C, and the successful fabrication of abundant heterogeneous interfaces. Nevertheless, only typical lattice fringes of single carbide phase can be indexed in either the Mo_2C-nws or the MoC-nws sample (Figure 1h,l). It is often found that in nanoelectrodes with rich interfaces and better electronic conductivity, both mass transport

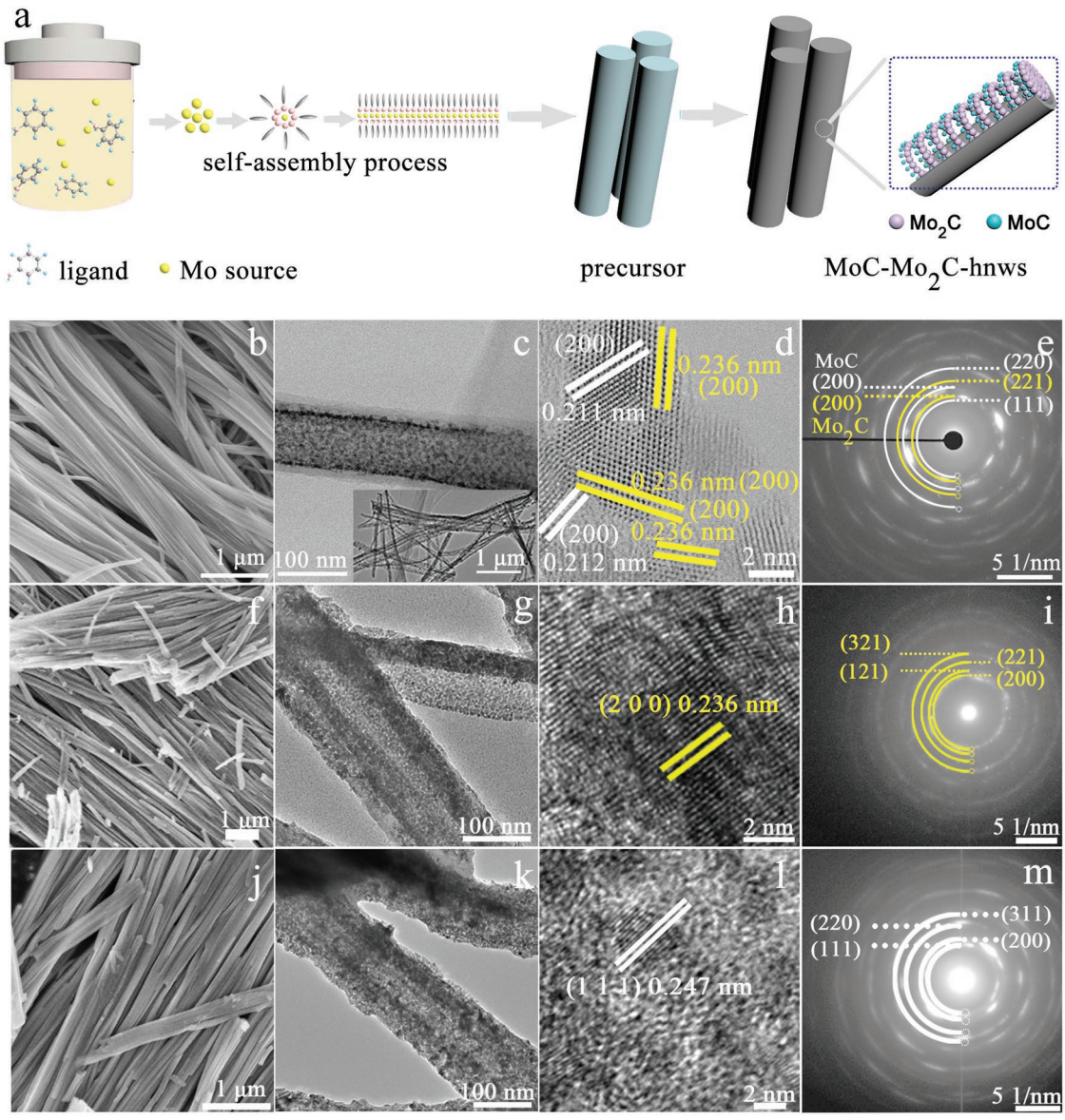

Figure 1. a) Schematic illustration of synthesis procedure for MoC-Mo_2C-hnws. b) The SEM image, c) TEM image, and d) high-resolution TEM images, and e) SAED pattern of MoC-Mo_2C-hnws. MoC phase highlighted in white and Mo_2C phase highlighted in yellow in (d) and (e). f) The SEM image, g) TEM image, and h) high-resolution TEM images, and i) SAED pattern of Mo_2C-nws. Mo_2C phase highlighted in yellow in (h) and (i). j) The SEM image, k) TEM image, and l) high-resolution TEM images, and m) SAED pattern of MoC-nws. MoC phase highlighted in white in (l) and (m).

process and redox reversibility could be facilitated due to the significantly reduced diffusion distances of electrons/ions.[37,38] Hence, it is anticipated that the heterogeneous interfaces and higher theoretical capacity of MoC-Mo_2C-hnws may bring forth enhanced electrochemical kinetics in comparison with the Mo_2C-nws counterpart. It is observed that MoC-Mo_2C-hnws contains a dense yet homogeneous population of MoC and Mo_2C nanoparticles on the carbon matrix and in all the as-prepared samples, the particle sizes of molybdenum-based species are identified to be ≈5 nm. Aside from this, the analysis of the selected area electron diffraction patterns (SAED, Figure 1e,i,m) demonstrated the polycrystallographic features of MoC-Mo_2C-hnws, MoC-nws, and Mo_2C-nws samples. The SAED pattern of MoC-Mo_2C-hnws reveals the characteristic d_{200}, d_{220}, and d_{111} spacing of MoC phase (highlighted in white color) and the d_{200} (d_{221}) spacing of Mo_2C phase (labeled in yellow color), confirming that the binary metal carbides are confined in the carbon matrix, which is in good accordance with the high-resolution TEM results.

Figure S2 (Supporting Information) and **Figure 2**a show the X-ray diffraction (XRD) patterns of the nanowire precursor and the freshly prepared samples. All Bragg reflections in Figure S2 (Supporting Information) demonstrate unambiguously that the $Mo_3O_{10}(C_6H_8N)_2 \cdot 2H_2O$ precursor crystallizes in monoclinic symmetry (P21/*(11)) with the following lattice parameters: a = 17.656 Å, b = 7.561 Å, and c = 16.282 Å (JCPDS No.

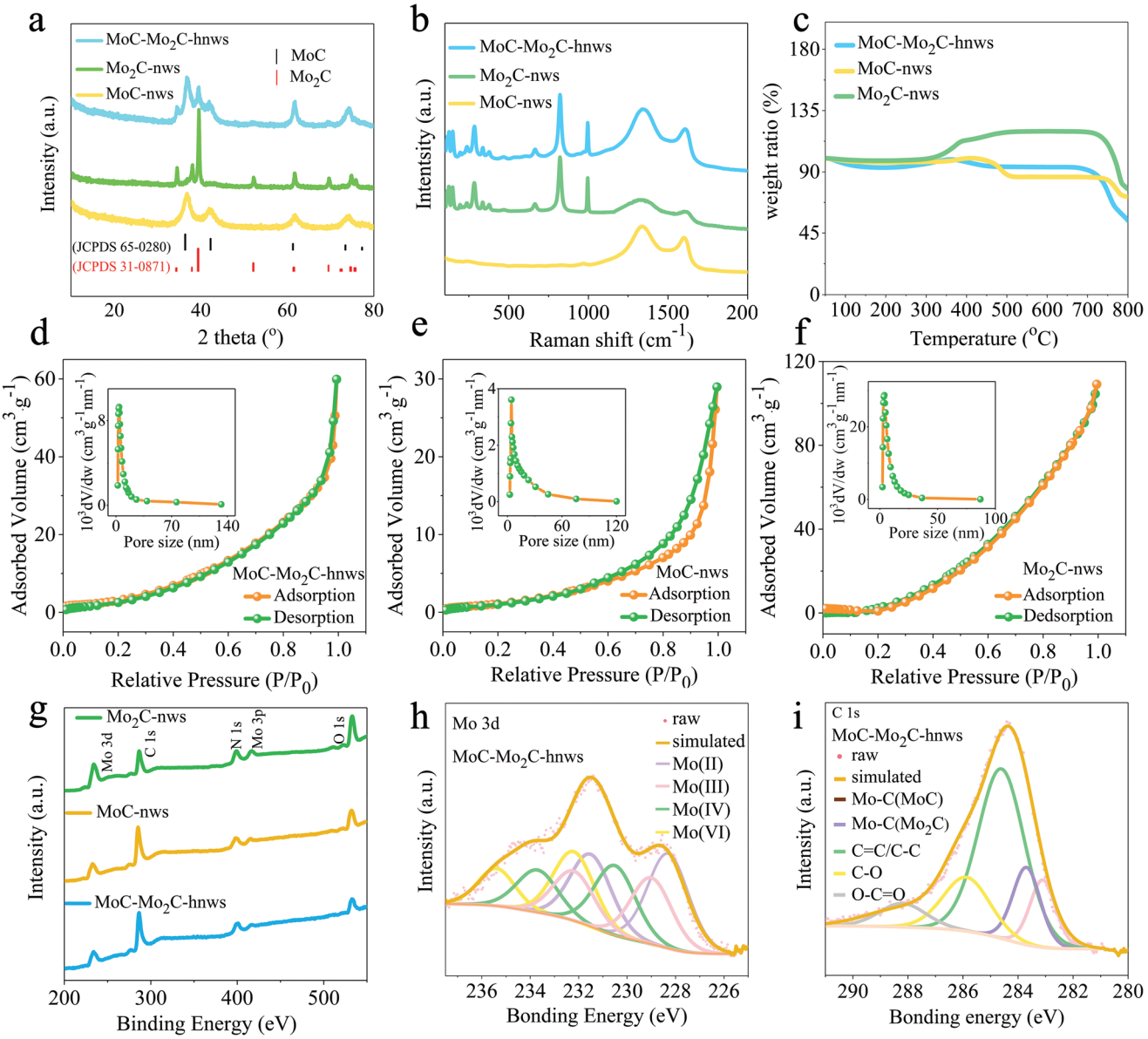

Figure 2. a) X-ray diffraction patterns of MoC-Mo_2C-hnws, Mo_2C-nws, and MoC-nws. b) Raman spectra of MoC-Mo_2C-hnws, Mo_2C-nws, and MoC-nws. c) Thermogravimetric analysis (TGA) of MoC-Mo_2C-hnws, Mo_2C-nws, and MoC-nws. d–f) Nitrogen adsorption and desorption isotherms and pore size distribution for MoC-Mo_2C-hnws, Mo_2C-nws, and MoC-nws. g) XPS survey spectra of MoC-Mo_2C-hnws, Mo_2C-nws, and MoC-nws. h) Mo 3d high-resolution XPS spectrum of MoC-Mo_2C-hnws. i) C 1s high-resolution XPS spectrum of MoC-Mo_2C-hnws.

50-2402), and within the detection limit, the absence of any visible impurities indicates the high phase purity of the precursor. For Mo_2C-nws, all peaks could be well indexed to the standard patterns of orthorhombic Mo_2C (space group: *Pbcn*, JCPDS No. 31-0871), and the strong diffraction peaks at 34.3°, 39.3°, and 52.1° match well with the (0 2 1), (1 2 1), and (2 2 1) planes of the Mo_2C lattice. Only cubic MoC (space group: *Fm-3m*, JCPDS No. 65-0280) was identified in MoC-nws with lattice parameters of a = 4.273 Å, b = 4.273 Å, and c = 4.273 Å, and the broad Bragg reflections suggest the poor crystallinity and amorphous state of the as-formed MoC nanoparticles. In comparison, the XRD pattern of MoC-Mo_2C-hnws comprises overlapping diffraction patterns of binary carbides (orthorhombic Mo_2C and cubic MoC), verifying the successful fabrication of MoC-Mo_2C-hnws heterostructures. Concomitantly, MoC-Mo_2C-hnws also shows broad Bragg reflections with respect to MoC phase, implying that the encapsulated MoC nanoparticles are less crystallized. This is similar to what was reported in most previous researches, wherein MoC specimens show weak crystallinity.[39] Moreover, Raman spectroscopy measurements ranging from 200 to 1000 cm^{-1} further confirmed the nearly amorphous nature of the as-formed MoC nanoparticles (Figure 2b), since the characteristic vibration modes of Mo-C(MoC) are almost invisible in the Raman spectrum of MoC-nws, and this has also been observed in MoC-Mo_2C-hnws after subtracting the typical narrow-band vibrations of crystalline Mo_2C. Furthermore, free

carbon reflections could be observed in the Raman patterns, with broadband peaks at ≈1300 and 1600 cm^{-1} exactly assigned to the D band and G band.[22] The intensity ratios of the D band to the G band were calculated as 1.9 (MoC-nws), 1.4 (Mo_2C-nws), and 2.3 (MoC-Mo_2C-hnws samples), manifesting that there are more lattice edges and amorphous states of carbon in the MoC-Mo_2C-hnws.[40] Interestingly, as some recent researches point out, disordered structures in the designed electrodes are beneficial to raise up ion and electron diffusivity, mainly because the amorphous structure has more defects/vacancies, and the percolation channels inside amorphous materials could potentially enhance the mass transport process within the active phases, and enable Li^+ diffusion to proceed more swiftly than in its crystalline counterparts.[41–43] For instance, Cao and co-workers reported that amorphous V_2O_5 exhibited better Na storage performances in comparison with the crystalline counterparts.[42] Tian et al. found an amorphous Li_2O_2 could deliver ionic conductivity up to 2×10^{-7} S cm^{-1}, nearly 12 orders of magnitude larger than the crystalline counterpart.[44] Thus, the engineering or integration with less crystallized MoC on the interfaces of Mo_2C is anticipated to promote the charge transfer kinetics and better rate performances. The Rietveld refinement analysis of MoC-Mo_2C-hnws has been conducted (Figure S3, Supporting Information) to investigate the structural details of MoC-Mo_2C-hnws. The structural parameters of MoC and Mo_2C are tabulated in Table S1 (Supporting Information), and the unit cells of the MoC and Mo_2C lattices are displayed in Figure S4 (Supporting Information). In orthorhombic Mo_2C crystals, the carbon atoms are located at the octahedral interstitial sites, while the molybdenum atoms are slightly deviated from occupying precise hexagonal close packed (hcp) sites.[45] Whereas, each Mo atom is surrounded by six C atoms in cubic MoC, showing a final structure similar to that of NaCl crystal. The as-prepared composites were further examined by thermogravimetric analysis (TGA), which was conducted from room temperature to 700 °C in air (Figure 2c). The whole process is comprised of two stages, where stage I (below 200 °C) represents the loss of physically absorbed water and stage II (from 200 to 700 °C) includes the carbon combustion (weight loss) and the phase transformation from molybdenum carbide to molybdenum trioxide (weight increase).[46]

Important as material dimensions and morphology, the porosity of electrodes also plays a significant role in influencing the electrochemical performances.[14] Therefore, the Brunauer–Emmett–Teller (BET) surface area and pore types of the as-prepared samples have been determined, as shown by the nitrogen adsorption–desorption isotherms in Figure 2d–f. MoC-nws displays a type IV isotherm, and both MoC-Mo_2C-hnws and Mo_2C-nws exhibit typical type III isotherms.[40] The BET surface areas of MoC-Mo_2C-hnws, Mo_2C-nws, and MoC-nws were found to be 57.8, 106.3, and 26.9 m^2 g^{-1}, respectively, and this porosity divergence of the products mainly originates from different carbothermal process. The pore size distribution has been calculated by the Barrett–Joyner–Halenda (BJH) method.[14] All samples show mesoporous features, showing pore sizes less than 20 nm (the insets of Figure 2d–f). Previous reports demonstrated that the as-displayed pore distribution range may mainly derive from particle interspaces, and some interstitial pores of the nanowire structure.[47,48] The unique porous structures of these products are promising to contribute to a better Li storage performance, since these nanopores could enhance the contact between electrode and electrolyte, alleviate strains during energy storage, and offer additional lithium storage sites, and such factors are anticipated to bring forth better electrochemical performance of the electrodes.[40]

X-ray photoelectron spectroscopy (XPS) was also performed to examine the composite configurations and chemical states of the samples (Figure 2g–i, Figure S5, Supporting Information). The overall XPS spectra consist of spectra for Mo and C elements (Figure 2g). Specifically, the Mo 3d core-level XPS high-resolution spectra demonstrate that there are four types of Mo oxidation valence states in MoC-Mo_2C-hnws, showing Mo^{2+}, Mo^{3+}, Mo^{4+}, and Mo^{6+} peaks with deconvoluted doublets at 231.6/228.3, 232.2/229, 233.7/230.5, and 235.7/232.2 eV, respectively. The identified Mo^{2+} and Mo^{3+} valence states were attributed to Mo_2C and MoC species, respectively, which is in accordance with the research by Lin et al.[49] The Mo^{4+} and Mo^{6+} states may mainly originate from partial oxidation of carbides in air, which are commonly reported for carbides.[49] In comparison, aside from some oxidation peaks, only the distinctive Mo^{3+} peak could be detected in MoC-nws, and Mo^{2+} species in Mo_2C-nws, respectively. It is known that conversion reaction based materials with lightweight and additional metal cation valences are beneficial for raising the theoretical capacity for lithium storage.[50] In addition to this, rich interfaces in nanoelectrodes could contribute to facilitating mass transport process and redox reversibility because of the significantly reduced diffusion distances of charge carriers.[37,38] Hence, it is anticipated that the heterogeneous interfaces and higher theoretical capacity of MoC-Mo_2C-hnws may bring forth superior electrochemical performances to the counterpart of Mo_2C-nws. With regard to the high-resolution C 1s spectra, all the samples showed peaks attributable to C=C/C–C (sp^2 carbon bonds, 284.6 eV), and some functional groups C–O (285.9 eV)/O–C=O (288.2 eV), revealing small differences in their carbonaceous networks.[51–53] In addition, Mo–C (MoC, 282.9 eV) and Mo–C (Mo_2C, 283.7 eV) bonds were individually observed in the MoC-nws and Mo_2C-nws samples, respectively,[51–53] and signals at 282.9/283.7 eV were both observed in MoC-Mo_2C-hnws. The above results demonstrate that these samples contain different Mo–C bonding modes and Mo chemical states, which may result in distinct electronic states and associated divergent anodic performances of the samples.[50]

To explore the effects of MoC integration with Mo_2C, the electrochemical performances of the samples pertaining to lithium storage were examined. The cyclic voltammetry (CV) profiles of MoC-Mo_2C-hnws were recorded at 0.1 mV s^{-1} (**Figure 3**a), as well as those of MoC-nws and Mo_2C-nws samples (Figure S6a,b, Supporting Information). In Figure 3a, irreversible reduction peaks appearing in the first cycle could be assigned to the side reactions with electrolyte and the generation of a solid-electrolyte interphase layer.[54] It should be noted that, in the second and third cycles of MoC-Mo_2C-hnws, the CV curves show well-overlapped shapes, and the area of the CV profile has increased in comparison with that of the first cycle, indicating the good Li^+ insertion/extraction reversibility of MoC-Mo_2C-hnws.[22] The galvanostatic charge/discharge profiles (Figure 3b) demonstrate that MoC-Mo_2C-hnws could afford an initial discharge capacity

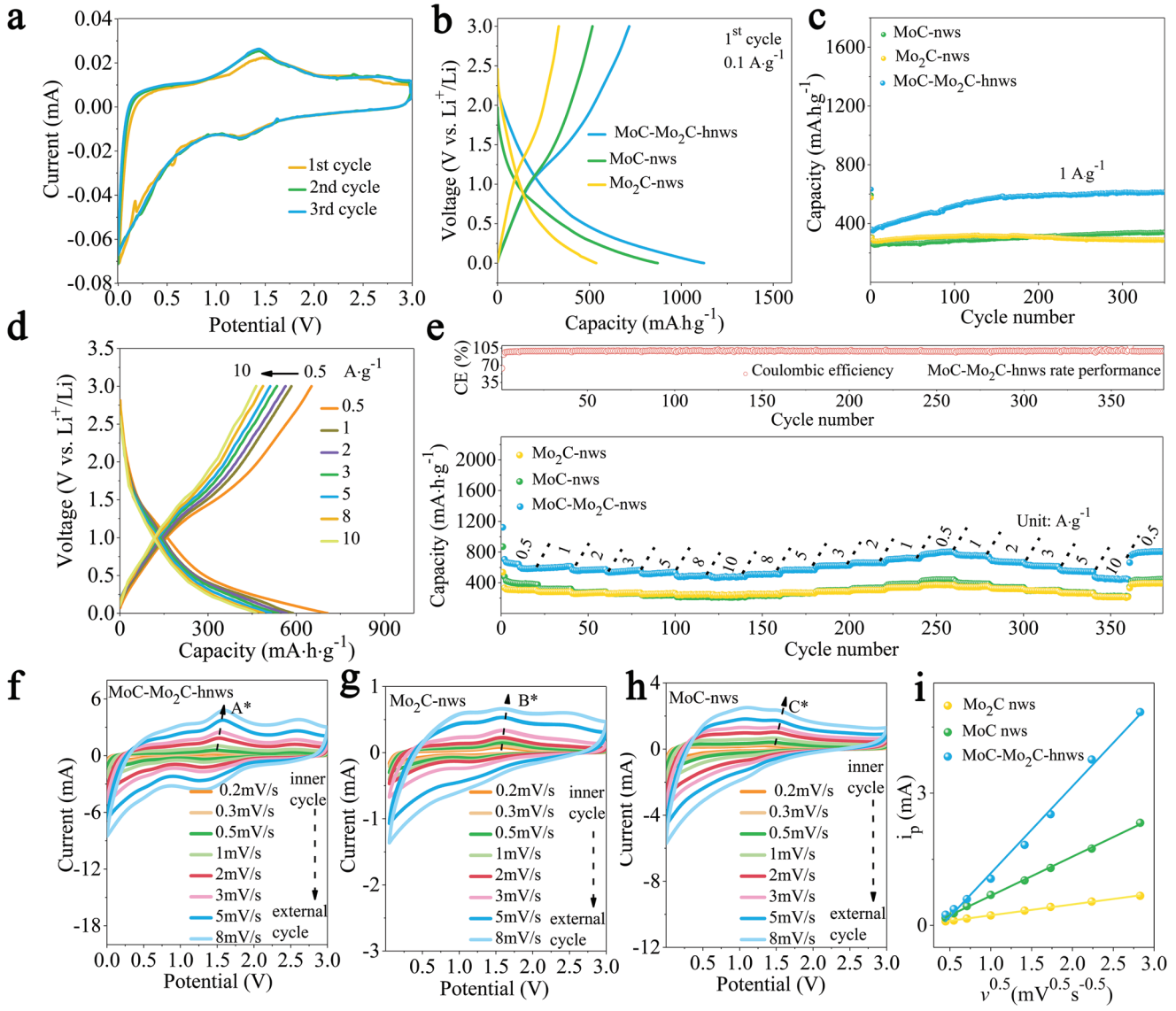

Figure 3. a) Cyclic voltammetry profiles of MoC-Mo_2C-hnws for the initial three cycles (scan rate = 0.1 mV s^{-1}). b) Comparison of the initial discharge/charge curves (100 mA g^{-1}) of MoC-Mo_2C-hnws, Mo_2C-nws, and MoC-nws electrodes. c) Long-term cycling performances of MoC-Mo_2C-hnws, Mo_2C-nws, and MoC-nws electrodes at 1 A g^{-1}. d) Discharge/charge curves of MoC-Mo_2C-hnws electrode at the current densities of 0.5, 1, 2, 3, 5, 8, and 10 A g^{-1}. e) (Top frame) The corresponding coulombic efficiency of the rate performance of MoC-Mo_2C-hnws electrode; (bottom frame) comparison of the rate performances of MoC-Mo_2C-hnws, Mo_2C-nws, and MoC-nws electrodes at 0.5, 1, 2, 3, 5, 8, 10 ,8, 5, 3, 2, 1, 0.5, 1, 2, 3, 5, 10, and 0.5 A g^{-1}, where the initial cycle was activated under the current density of 0.1 A g^{-1}. CV curves at different scan rates of f) MoC-Mo_2C-hnws, g) Mo_2C-nws, and h) MoC-nws. i) Linear relationship of peak currents versus $mV^{0.5}$ $s^{-0.5}$ and the corresponding linear fits for MoC-Mo_2C-hnws, Mo_2C-nws, and MoC-nws electrodes. The data of peak currents are extracted from A* in (f), B* in (g), and C* in (h).

of ≈1120 mA h g^{-1}, and achieve a higher initial Coulombic efficiency (ICE) (≈64%) in comparison with the ICE values of MoC-nws (≈59%) and Mo_2C-nws (≈57%). The initial capacity loss should be attributed to the irreversible side reactions or electrolyte decomposition.[55] The higher ICE values of hetero-electrodes suggest that component interactions between MoC and Mo_2C may contribute mainly to enhancing the initial lithiation/delithiation reversibility, which presumably be attributed to a facilitated heterocharge transfer among the active phases, uniquely induced by the hybrid structure.[55,56] Figure 3c shows that MoC-nws, Mo_2C-nws, and MoC-Mo_2C-hnws could retain an average discharge capacity of ≈340, 280, and 610 mA h g^{-1} after 350 cycles at 1 A g^{-1}, respectively. This indicates better lithium storage performance in heterocomposites than samples with single molybdenum component (MoC-nws, Mo_2C-nws). A capacity increment could be observed in the long-term cycling of MoC-Mo_2C-hnws, which may mainly benefit from the enhanced surface/near-surface reactions stemming from the abundant heterointerfaces and amorphous nature of MoC interface layer, as often reported in conversion-type electrodes.[22]

We further evaluated the rate performance and stability of the designed heteroelectrode. Figure 3d,e shows the

electrochemical performances of MoC-nws, Mo_2C-nws, and MoC-Mo_2C-hnws under alternating C-rates. MoC-Mo_2C-hnws exhibit average discharge capacities of ≈640, 610, 560, 560, 520, 490, and 470 mA h g^{-1} at 0.5, 1, 2, 3, 5, 8, and 10 A g^{-1}, respectively, with nearly 100% Coulombic efficiency (CE). When the current density was switched back to 8, 5, 3, 2, 1, and 0.5 A g^{-1}, the discharge capacities were retained with no obvious fading. Impressively, a similar case reoccurred when the electrode was tested repeatedly using C-rates of 1, 2, 3, 5, and 10 A g^{-1} after 260 cycles. Following the former repeated high-rate testing, an average discharge capacity of ≈790 mA h g^{-1} was achieved by MoC-Mo_2C-hnws over 380 cycles at 0.5 A g^{-1}. The MoC-Mo_2C-hnws had 2.3 (1.9)-fold higher capacities than Mo_2C-nws (MoC-nws), and the highest specific capacity over the whole cycling test confirmed that a superior structure was achieved by the design of the MoC-Mo_2C-hnws materials. The as-prepared MoC-Mo_2C-hnws electrodes show impressive rate duration performance and higher rate capacity, illustrating that heterostructure-functionalized carbides have great potential to meet the increasing demands of high-power lithium-ion batteries.

To gain a further insight into the detailed lithium storage mechanisms of the as-prepared samples, we investigated the electrochemical reaction kinetics in detail in the following. The Nyquist profiles (Figure S6c, Supporting Information) obtained from electrochemical impedance spectroscopy (EIS) illustrate the different resistances of MoC-nws, Mo_2C-nws, and MoC-Mo_2C-hnws after 100 cycles. These samples exhibit similar resistance profiles, which show two depressed semicircles in the high and middle-frequency regions related to the solid-electrolyte resistance, and the charge transfer process, and a sloping line in the low-frequency region correlated with the solid-state Li^+ mass transfer process.[24] It is revealed that MoC-Mo_2C-hnws possess lower charge-transfer resistance (Table S1, Supporting Information) and lithium-ion diffusion resistance than MoC-nws and Mo_2C-nws, manifesting that a beneficial heterogeneous charge transfer and better electron/ion transport capabilities could be achieved in heterostructured electrodes. Furthermore, the morphological features of MoC-Mo_2C-hnws, Mo_2C-nws, and MoC-nws after cycling have been shown in Figure S7 (Supporting Information). As can be seen from these TEM images, the as-prepared samples show well-maintained nanowire morphologies, indicating the robust matrix and superior 1D nanowire structure of the as-prepared samples during cycling. Moreover, the effects of structures on lithium diffusion behaviors of these carbide-based electrodes were examined by Randles–Sevcik evaluations and galvanostatic intermittent titration methods. Figure 3f–i presents the CV profiles of MoC-nws, Mo_2C-nws, and MoC-Mo_2C-hnws at scan rates ranging from 0.2 to 8 mV s^{-1}. As the scan rate increases, it is observed that the peak intensities of the tested samples increase simultaneously, with a quick signal feedback to the increased scan rate, and all samples show well-preserved CV shapes. As the discharge and charge reaction rates are highly dependent on the ion diffusion process,[57] the Li^+ diffusion coefficients (D_{Li+}) were compared based on the Randles–Sevcik equation (Equation (1))

$$i_p = 0.4463nFAC\sqrt{\frac{nFDv}{RT}} \quad (1)$$

In this equation, i_p, D, n, A, and v correspond to the intensity of the peak current, the diffusion coefficient, the number of electrons, the surface area of the electrodes, and the voltage scan rate, respectively. F, T, and R refer to the Faraday constant, the absolute temperature during the testing, and the gas constant, respectively. C is the concentration of Li^+. Since all tested electrodes and cells were fabricated by the same procedure, the Randles–Sevcik equation to calculate Li^+ diffusion coefficient could be simplified as Equation (2)[57]

$$i_p = k\sqrt{D}\sqrt{v} \quad (2)$$

in which, k is considered to be a constant in lithium-ion batteries, and the Li^+ diffusion coefficient could be redefined as $kD^{1/2}$, which could be obtained from the linear relationship between the peak current (i_p: A*/B*/C*) and the square root of the scan rates ($v^{1/2}$). As clearly seen, the Li^+ diffusion process of MoC-nws has been proved to be more efficient than that of Mo_2C-nws. On the other hand, being a composite of MoC and Mo_2C electroactive phases, MoC-Mo_2C-hnws showed a further enhanced diffusion coefficient in comparison with MoC-nws and Mo_2C-nws. This phenomenon is also consistent with the results of GITT measurements. Figure S8 (Supporting Information) compares the lithium diffusion coefficients of MoC-Mo_2C-hnws, Mo_2C-nws, and MoC-nws. The facilitated lithium diffusion capability in MoC-Mo_2C-hnw rationally interprets the superior long-term cycling stability and excellent high-rate capability of MoC-Mo_2C-hnws, which outperforms those of other reported molybdenum carbide based electrodes as shown in **Figure 4**a. The kinetics analysis has verified the effects of the heterostructures toward the superior rate performance of MoC-Mo_2C-hnws by facilitating both electron and Li^+ mobility among the electrode materials, since heterodesigns may induce the formation of implanted electric fields and more delocalized charge transport among the available active sites,[27,28,61] benefited from which, the transport of charge carriers could be accelerated thus producing improved electrochemical reactivity with lithium and fast high-rate response (Figure 4b). In summary, disproportionation reaction assisted method has useful application in preparing heterostructures and advanced energy storage materials, which could further modulate the physicochemical properties of compounds. As investigated in this work, the accelerated electron and ion mobility and strong component interaction reinforced the lithium storage in the well-fabricated MoC-Mo_2C-hnws, guarantees its stable high-rate performances with no significant fading and enables its further application as a high-rate performance electrode. Such improvements manifest that heterostructure provides a facile and general strategy to achieve high-rate carbide electrodes for advanced electrochemical energy storage.

In this work, heterostructured MoC-Mo_2C-hnws electrode has been fabricated as an advanced high-rate performance anode for LIBs. The stoichiometry tunable heteromolybdenum carbide anode exhibited improved lithium storage capability as well as electrochemical reactivity with lithium in comparison with its individual counterparts. Several advantages are summarized. First, the carbon nanowire matrix plays a significant role in this remarkable lithium storage

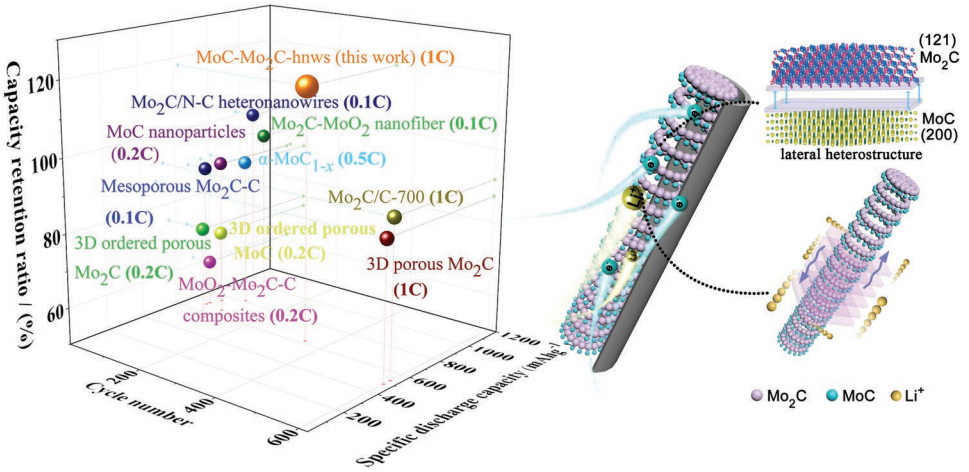

Figure 4. The possible lithium storage mechanisms of MoC-Mo_2C-hnws electrode.[18–20,24,36,58–60]

performance, which could prevent the agglomeration of the active phases of MoC and Mo_2C nanoparticles, function as an electron conductive highway and carbon sheath to accommodate the volumetric variations of active phase, so that it contributes significantly to the cycling stability of the MoC-Mo_2C-hnws electrode. Furthermore, the heterostructures have shown to alter the interfacial kinetics, giving rise to accelerated transport of mass and charge carriers, making MoC-Mo_2C-hnws as a promising high-rate performance electrode. This work highlights the significance of superior structural designs in improving electrochemical energy storage, and the proposed stoichiometry-tunable strategy may open up a new way to improve the properties of other carbide-based materials and reveal their full potential as advanced anodes for next-generation high-power LIBs.

Supporting Information

Supporting Information is available from the Wiley Online Library or from the author.

Acknowledgements

This work was partially supported by the National Science Fund for Distinguished Young Scholars (Grant No. 51625102), the National Natural Science Foundation of China (Grant Nos. 51471053 and 51802357), the Science and Technology Commission of Shanghai Municipality (Grant No. 17XD1400700), Hubei Provincial Natural Science Foundation of China (2018CFB237), and the Fundamental Research Funds for the Central Universities (CZT19003). Also, financial support provided by the Australian Research Council (ARC) (Grant Nos. LP160101629, FT150100109, and DE190100504) are gratefully acknowledged. The authors thank the Electron Microscopy Centre (EMC) at the University of Wollongong. The authors also thank Dr. T. Silver for critical reading of the manuscript.

Conflict of Interest

The authors declare no conflict of interest.

Keywords

anodes, carbon rich, heterostructures, lithium-ion battery, molybdenum carbide

Received: July 10, 2019
Revised: August 28, 2019
Published online: September 17, 2019

[1] a) A. S. Arico, P. Bruce, B. Scrosati, J. M. Tarascon, W. Van Schalkwijk, *Materials for Sustainable Energy: A Collection of Peer-Reviewed Research and Review Articles from Nature Publishing Group*, World Scientific, Singapore **2011**, p. 148; b) T. Zhou, Y. Zheng, H. Gao, S. Min, S. Li, H. Liu, Z. Guo, *Adv. Sci.* **2015**, *2*, 1500027; c) S. Hu, Y. Li, Y. Chen, J. Peng, T. Zhou, W. K. Pang, C. Didier, V. K. Peterson, H. Wang, Q. Li, Z. Guo, *Adv. Energy Mater.* **2019**, 1901795.
[2] Y. G. Guo, J. S. Hu, L. J. Wan, *Adv. Mater.* **2008**, *20*, 2878.
[3] a) Z. Yang, J. Zhang, M. C. Kintner-Meyer, X. Lu, D. Choi, J. P. Lemmon, J. Liu, *Chem. Rev.* **2011**, *111*, 3577; b) J. R. He, A. Manthiram, *Energy Storage Mater.* **2019**, *20*, 55; c) J. R. He, Y. F. Chen, A. Manthiram, *Adv. Energy Mater.* **2019**, *9*, 1900584.
[4] D. Yu, C. Chen, S. Xie, Y. Liu, K. Park, X. Zhou, Q. Zhang, J. Li, G. Cao, *Energy Environ. Sci.* **2011**, *4*, 858.
[5] C. Zhu, X. Mu, P. A. van Aken, Y. Yu, J. Maier, *Angew. Chem., Int. Ed.* **2014**, *53*, 2152.
[6] G. N. Zhu, Y. G. Wang, Y. Y. Xia, *Energy Environ. Sci.* **2012**, *5*, 6652.
[7] N. S. Choi, Z. Chen, S. A. Freunberger, X. Ji, Y. K. Sun, K. Amine, G. Yushin, L. F. Nazar, J. Cho, P. G. Bruce, *Angew. Chem., Int. Ed.* **2012**, *51*, 9994.
[8] H. Li, Z. Wang, L. Chen, X. Huang, *Adv. Mater.* **2009**, *21*, 4593.
[9] a) H. Liu, G. Wang, J. Liu, S. Qiao, H. Ahn, *J. Mater. Chem.* **2011**, *21*, 3046.; b) C. X. Hou, Y. Hou, Y. Fan, Y. Zhai, Y. Wang, Z. Sun, R. Fan, F. Dang, J. Wang, *J. Mater. Chem. A* **2018**, *6*, 6967; c) C. X. Hou, Z. X. Tai, L. Zhao, Y. Zhai, Y. Hou, Y. Fan, F. Dang, J. Wang, H. Liu, *J. Mater. Chem. A* **2018**, *6*, 9723.
[10] S. W. Lee, N. Yabuuchi, B. M. Gallant, S. Chen, B. S. Kim, P. T. Hammond, Y. Shao-Horn, *Nat. Nanotechnol.* **2010**, *5*, 531.
[11] V. Etacheri, R. Marom, R. Elazari, G. Salitra, D. Aurbach, *Energy Environ. Sci.* **2011**, *4*, 3243.
[12] J. Meng, H. Guo, C. Niu, Y. Zhao, L. Xu, Q. Li, L. Mai, *Joule* **2017**, *1*, 522.
[13] F. Cheng, J. Liang, Z. Tao, J. Chen, *Adv. Mater.* **2011**, *23*, 1695.
[14] H. Song, J. Su, C. Wang, *ACS Appl. Mater. Interfaces* **2018**, *1*, 5008.

[15] V. Augustyn, J. Come, M. A. Lowe, J. W. Kim, P. L. Taberna, S. H. Tolbert, H. D. Abruna, P. Simon, B. Dunn, *Nat. Mater.* **2013**, *12*, 518.
[16] C. J. Zhang, S. J. Kim, M. Ghidiu, M. Q. Zhao, M. W. Barsoum, V. Nicolosi, Y. Gogotsi, *Adv. Funct. Mater.* **2016**, *26*, 4143.
[17] a) Q. Sun, Y. Dai, Y. Ma, T. Jing, W. Wei, B. Huang, *J. Phys. Chem. Lett.* **2016**, *7*, 937; b) C. X. Hou, J. Wang, W. Du, J. Wang, Y. Du, C. Liu, J. Zhang, H. Hou, F. Dang, L. Zhao, *J. Mater. Chem. A* **2019**, *7*, 13460; c) H. J. Zhang, K. X. Wang, X. Y. Wu, Y. M. Jiang, Y. B. Zhai, C. Wang, X. Wei, J. S. Chen, *Adv. Funct. Mater.* **2014**, *24*, 3399; d) B. Yu, D. X. Yang, Y. Hu, J. R. He, Y. F. Chen, W. D. He, *Small Methods* **2019**, *3*, 1800287.
[18] W. Tian, H. Hu, Y. Wang, P. Li, J. Liu, J. Liu, X. Wang, X. Xu, Z. Li, Q. Zhao, H. Ning, W. Wu, M. Wu, *ACS Nano* **2018**, *12*, 1990.
[19] H. Yu, H. Fan, J. Wang, Y. Zheng, Z. Dai, Y. Lu, J. Kong, X. Wang, Y. J. Kim, Q. Yan, J. M. Lee, *Nanoscale* **2017**, *9*, 7260.
[20] T. Meng, L. Zheng, J. Qin, D. Zhao, M. Cao, *J. Mater. Chem. A* **2017**, *5*, 20228.
[21] K. Kang, Y. S. Meng, J. Bréger, C. P. Grey, G. Ceder, *Science* **2006**, *311*, 977.
[22] C. Zhao, C. Yu, B. Qiu, S. Zhou, M. Zhang, H. Huang, B. Wang, J. Zhao, X. Sun, J. Qiu, *Adv. Mater.* **2018**, *30*, 1702486.
[23] L. Yang, X. Li, S. He, G. Du, X. Yu, J. Liu, Q. Gao, R. Hu, M. Zhu, *J. Mater. Chem. A* **2016**, *4*, 10842.
[24] Q. Gao, X. Zhao, Y. Xiao, D. Zhao, M. Cao, *Nanoscale* **2014**, *6*, 6151.
[25] R. Li, S. Wang, W. Wang, M. Cao, *Phys. Chem. Chem. Phys.* **2015**, *17*, 24803.
[26] a) B. Wang, G. Wang, H. Wang, *J. Mater. Chem. A* **2015**, *3*, 17403; b) J. R. He, G. Hartmann, M. Lee, G. S. Hwang, Y. F. Chen, A. Manthiram, *Energy Environ. Sci.* **2019**, *12*, 344.
[27] K. Chen, X. Wang, G. Wang, B. Wang, X. Liu, J. Bai, H. Wang, *Chem. Eng. J.* **2018**, *347*, 552.
[28] A. Nourbakhsh, A. Zubair, M. S. Dresselhaus, T. s. Palacios, *Nano Lett.* **2016**, *16*, 1359.
[29] J. Zhang, L. Sun, Y. Zhou, P. Peng, *Comput. Mater. Sci.* **2015**, *98*, 211.
[30] L. Wang, X. Gu, L. Zhao, B. Wang, C. Jia, J. Xu, Y. Zhao, J. Zhang, *Electrochim. Acta* **2019**, *295*, 107.
[31] Y. Jing, X. Mu, C. Xie, H. Liu, R. Yan, H. Dai, C. Liu, X. D. Zhang, *Int. J. Hydrogen Energy* **2019**, *44*, 809.
[32] K. X. Wang, X. H. Li, J. S. Chen, *Adv. Mater.* **2015**, *27*, 527.
[33] X. Hong, J. Kim, S. F. Shi, Y. Zhang, C. Jin, Y. Sun, S. Tongay, J. Wu, Y. Zhang, F. Wang, *Nat. Nanotechnol.* **2014**, *9*, 682.
[34] K. Fan, T. Tang, S. Wu, Z. Zhang, *I. J. Mod. Phys. B* **2018**, *32*, 1850010.
[35] T. Yu, Z. Zhao, L. Liu, S. Zhang, H. Xu, G. Yang, *J. Am. Chem. Soc.* **2018**, *140*, 5962.
[36] M. Li, S. Yu, Z. Chen, Z. Wang, F. Lv, B. Nan, Y. Zhu, Y. Shi, W. Wang, S. Wu, H. Liu, Y. Tang, Z. Lu, *Inorg. Chem. Front.* **2017**, *4*, 289.
[37] F. Wang, R. Robert, N. A. Chernova, N. Pereira, F. Omenya, F. Badway, X. Hua, M. Ruotolo, R. Zhang, L. Wu, *J. Am. Chem. Soc.* **2011**, *133*, 18828.
[38] J. Cabana, L. Monconduit, D. Larcher, M. R. Palacin, *Adv. Mater.* **2010**, *22*, E170.
[39] C. Wan, N. A. Knight, B. M. Leonard, *Chem. Commun.* **2013**, *49*, 10409.
[40] Y. Yang, M. Luo, Y. Xing, S. Wang, W. Zhang, F. Lv, Y. Li, Y. Zhang, W. Wang, S. Guo, *Adv. Mater.* **2018**, *30*, 1706085.
[41] J. Lee, A. Urban, X. Li, D. Su, G. Hautier, G. Ceder, *Science* **2014**, *343*, 519.
[42] E. Uchaker, Y. Z. Zheng, S. Li, S. L. Candelaria, S. Hu, G. Z. Cao, *J. Mater. Chem. A* **2014**, *2*, 18208.
[43] J. H. Ku, J. H. Ryu, S. H. Kim, O. H. Han, S. M. Oh, *Adv. Funct. Mater.* **2012**, *22*, 3658.
[44] F. Tian, M. D. Radin, D. J. Siegel, *Chem. Mater.* **2014**, *26*, 2952.
[45] H. H. Hwu, J. G. Chen, *Chem. Rev.* **2005**, *105*, 185.
[46] Y. Huang, Q. Gong, X. Song, K. Feng, K. Nie, F. Zhao, Y. Wang, M. Zeng, J. Zhong, Y. Li, *ACS Nano* **2016**, *10*, 11337.
[47] Y. Zhang, C. Wang, H. Hou, G. Zou, X. Ji, *Adv. Energy Mater.* **2017**, *7*, 1600173.
[48] T. Zhou, Y. Zheng, H. Gao, S. Min, S. Li, H. K. Liu, Z. Guo, *Adv. Sci.* **2015**, *2*, 1500027.
[49] H. Lin, Z. Shi, S. He, X. Yu, S. Wang, Q. Gao, Y. Tang, *Chem. Sci.* **2016**, *7*, 3399.
[50] S. Wang, L. Li, Y. Shao, L. Zhang, Y. Li, Y. Wu, X. Hao, *Adv. Mater.* **2019**, *31*, 1806088.
[51] Y. S. Ye, Y. N. Chen, J. S. Wang, J. Rick, Y. J. Huang, F. C. Chang, B. J. Hwang, *Chem. Mater.* **2012**, *24*, 2987.
[52] G. Gao, D. Liu, S. Tang, C. Huang, M. He, Y. Guo, X. Sun, B. Gao, *Sci. Rep.* **2016**, *6*, 20034.
[53] J. Qiu, Z. Yang, Q. Li, Y. Li, X. Wu, C. Qi, Q. Qiao, *J. Mater. Chem. A* **2016**, *4*, 13296.
[54] X. Zhao, H. E. Wang, X. Chen, J. Cao, Y. Zhao, Z. G. Neale, W. Cai, J. Sui, G. Cao, *Energy Storage Mater.* **2018**, *11*, 161.
[55] Y. Liu, X. Y. Yu, Y. Fang, X. Zhu, J. Bao, X. Zhou, X. W. Lou, *Joule* **2018**, *2*, 725.
[56] X. Zhou, L. Yu, X. W. D. Lou, *Adv. Energy Mater.* **2016**, *6*, 1600451.
[57] J. Qin, T. Wang, D. Liu, E. Liu, N. Zhao, C. Shi, F. He, L. Ma, C. He, *Adv. Mater.* **2018**, *30*, 1704670.
[58] H. Li, H. Ye, Z. Xu, C. Wang, J. Yin, H. Zhu, *Phys. Chem. Chem. Phys.* **2017**, *19*, 2908.
[59] L. Yang, X. Li, Y. Ouyang, Q. Gao, L. Ouyang, R. Hu, J. Liu, M. Zhu, *ACS Appl. Mater. Interfaces* **2016**, *8*, 19987.
[60] Y. Zhu, S. Wang, Y. Zhong, R. Cai, L. Li, Z. Shao, *J. Power Sources* **2016**, *307*, 552.
[61] R. Comes, S. Chambers, *Phys. Rev. Lett.* **2016**, *117*, 226802.